Determination of Vega's rotational velocity based on the Fourier analysis of spectral line profiles

Yoichi Takeda [ID]★

11-2 Enomachi, Naka-ku, Hiroshima-shi 730-0851, Japan

ABSTRACT

While it is known that the sharp-line star Vega ($v_e \sin i \sim 20$ km s^{-1}) is actually a rapid rotator seen nearly pole-on with low i ($<10°$), no consensus has yet been accomplished regarding its intrinsic rotational velocity (v_e), for which rather different values have been reported so far. Methodologically, detailed analysis of spectral line profiles is useful for this purpose, since they reflect more or less the v_e-dependent gravitational darkening effect. However, direct comparison of observed and theoretically simulated line profiles is not necessarily effective in practice, where the solution is sensitively affected by various conditions and the scope for combining many lines is lacking. In this study, determination of Vega's v_e was attempted based on an alternative approach making use of the first zero (q_1) of the Fourier transform of each line profile, which depends on K (temperature sensitivity parameter differing from line to line) and v_e. It turned out that v_e and $v_e \sin i$ could be separately established by comparing the observed q_1^{obs} and calculated q_1^{cal} values for a number of lines of different K. Actually, independent analysis applied to two line sets (49 Fe I lines and 41 Fe II lines) yielded results reasonably consistent with each other. The final parameters of Vega's rotation were concluded as $v_e \sin i = 21.6(\pm0.3)$ km s^{-1}, $v_e = 195(\pm15)$ km s^{-1}, and $i = 6.4(\pm0.5)°$.

Key words: line: profiles – stars: atmospheres – stars: early-type – stars: individual (Vega) – stars: rotation.

1 INTRODUCTION

The spectrum of Vega ($=\alpha$ Lyr $=$ HR 7001 $=$ HD 172167 $=$ HIP 91262; spectral type A0 V) shows a sharp-line nature indicating a small projected rotational velocity ($v_e \sin i \sim 20$ km s^{-1}, where v_e is the equatorial rotation velocity and i is the angle of rotational axis relative to the line of sight), which is rather unusual among A-type main-sequence stars (many of them showing $v_e \sin i$ typically around ~100–300 km s^{-1}). It is nowadays known, however, that this star is actually a rapid rotator with large v_e like other A stars and the apparent smallness of $v_e \sin i$ is simply ascribed to low i (i.e. this star happens to be seen nearly pole-on).

Its intrinsic rotational velocity can be observationally determined by detecting the gravity darkening effect, because it becomes more exaggerated as v_e increases. The mainstream approach used for this purpose is to analyse the shape of spectral lines, because lines of a specific group (e.g. weak Fe I lines) show a characteristic feature (i.e. flat-bottomed profile), which is caused by the lowered temperature near to the gravity-darkened limb (see e.g. fig. 1 in Takeda, Kawanomoto & Ohishi 2008a). Alternatively, in order to establish v_e, the extent of gravity darkening can be estimated from the brightness distribution on the stellar disc by direct high-resolution interferometric observations.

Beginning from 1990s and especially in the period around 2010, quite a few determinations of Vega's v_e based on these two methods have been tried by various investigators as summarised in Table 1. However, the resulting literature values of v_e considerably differ from

each other as seen from this table. Although the large discrepancy amounting to $\gtrsim100$ km s^{-1} (from ~160 to ~270 km s^{-1}) seen in early 2000s has been mitigated up to the present, they are still diversified between ~170 and ~230 km s^{-1} (which are the published results since 2008).

Meanwhile, the discovery of magnetic field in Vega by spectropolarimetry (Lignières et al. 2009) provided a new means to measure v_e, because such a Zeeman signature would show cyclic variation due to rotation; that is, the rotational period (P) may be directly evaluated by applying a period analysis to time-series data of spectropolarimetric observations, from which v_e is derived as $v_e = 2\pi R_e/P$ by using an appropriately assigned R_e (equatorial radius). Following this policy, Vega's rotation period was determined within several years after 2010, as shown in Table 1. Although this method is expected to establish P precisely, these published data are not necessarily in good agreement but somewhat discrepant by $\sim\pm10$ per cent (i.e. $\sim\pm20$ km s^{-1} around $v_e \sim 200$ km s^{-1}). Therefore, even such an independent technique (which is essentially different from the other in the sense that any modelling of gravity-darkened star is not required) has not yet significantly improved the situation regarding the ambiguity in v_e.

Accordingly, it is desirable to redetermine v_e of Vega with higher reliability than before, in order to clarify which of the recent results (between 'low-scale' value of ~170–180 km s^{-1} and 'high-scale' value of ~220–230 km s^{-1}) is more justifiable.

Here, it may be worthwhile to mention the weak point of line profile analysis, which was once employed by the author's group (Takeda, Kawanomoto & Ohishi 2008b; hereinafter referred to as Paper I) to evaluate Vega's v_e. According to our experience, to derive v_e by searching for the best fit (minimising χ^2) between the observed

Table 1. Previous determinations of Vega's rotation and related parameters.

Authors	$v_e \sin i$ (km s^{-1})	v_e (km s^{-1})	i (deg)	R_p (R$_\odot$)	R_e (R$_\odot$)	P (d)	Remark
Gulliver et al. (1994)	21.8	245	5.1	–	–	–	Line profile
Hill et al. (2004)	21.9	160	7.9	–	–	–	Line profile
Aufdenberg et al. (2006)	21.9	270	4.7	2.26	2.78	–	Interferometry
Peterson et al. (2006)	21.5	274	4.5	2.31	2.87	–	Interferometry
Takeda et al. (2008b)	22[a]	175	7.2	2.52	2.76	–	Line profile
Yoon et al. (2010)	20.5	236	5.0	2.36	2.82	–	Line profile
Hill et al. (2010)	20.8	211	5.7	2.40	2.75	–	Line profile
Monnier et al. (2012)	21.3	197	6.2	2.42	2.73	–	Interferometry (their Model 3)
Petit et al. (2010)	–	184[b]	–	–	–	0.732	Magnetic modulation
Alina et al. (2012)	–	198[b]	–	–	–	0.678	Magnetic modulation
Butkovskaya (2014)	–	216[b]	–	–	–	0.623	Magnetic modulation
Böhm et al. (2015)	–	198[b]	–	–	–	0.678	Magnetic modulation

Notes. In columns 2–7 are given the values of projected rotational velocity, equatorial rotational velocity, inclination angle of rotational axis, polar radius, equatorial radius, and rotation period, respectively.
[a]Assumed value.
[b]Derived from P by assuming $R_e = 2.8$ R$_\odot$.

and modelled line profiles for a selected line feature (e.g. well-behaved weak Fe I line showing a flat-bottomed profile) is not so hard. However, there is no way to estimate how much uncertainty is involved in such a specific solution. Actually, since χ^2 residual is a rather broad function of v_e and quite vulnerable to a slight imperfection (e.g. improper placement of continuum level, existence of weak line blending, irregular noise in observed data, etc.), because extremely subtle difference of profile shape is concerned (typically of the order of $\sim 10^{-3}$ in unit of the continuum; cf. figs 4 and 5 in Paper I), an erroneous v_e solution is easily brought about (or even no solution is found). Therefore, it was decided in Paper I to analyse the profiles of a large number of lines (87 lines of neutral species and 109 lines of once-ionized species) with a hope of hitting as many correct solutions as possible. Nevertheless, from a critical point of view, the result obtained in Paper I was not very satisfactory due to the following reasons: (i) The final solution ($v_e = 175$ km s^{-1}) was simply selected from nine models (where v_e was varied from 100 to 300 km s^{-1} with an increment of 25 km s^{-1}) as the one corresponding to the highest frequency of χ^2 minimum for the case of neutral lines, so an ambiguity of ~ 20 km s^{-1} due to the coarseness of model grid is inevitable from the start. (ii) While lines of neutral species yielded a Gaussian-like frequency histogram centred around 175 km s^{-1} (cf. fig. 6a in Paper I), those of ionized species (many of them have 'non-flat-bottom' profiles) show a near-flat distribution (cf. fig. 6b in Paper I); this means that the latter set of ionized lines were almost useless because they made no contribution to the determination of v_e.

Consequently, the conventional line-profile matching in the wave-length domain applied in Paper I was not necessarily suitable for such a very delicate problem. In order to make a further step towards improving the precision, a more efficient approach has to be invoked, in which many lines of different properties can be effectively combined to increase the reliability of v_e solution while providing a reasonable procedure for error estimation.

Recently, in an attempt to estimate the intrinsic rotational velocity of Sirius A, Takeda (2020; hereinafter referred to as Paper II) made use of the first zero frequency (q_1) in the Fourier transform of the line profile. It then revealed that this quantity can be used for measuring the gravity darkening effect because it sensitively responds to a slight variation of the line profile; actually, q_1 was found to vary almost monotonically with v_e (inducing a gravity

darkening). While how q_1 reflects a change of v_e naturally differs from line to line depending on its property, it was found to be the sensitivity of line strength (W) to temperature (T), which is represented by the parameter K ($\equiv \log W/\log T$), that essentially controls the v_e dependence of q_1. Therefore, since information of v_e may be extracted from the comparison of the observed q_1^{obs} with a corresponding set of q_1^{cal} (K, v_e) calculated for this line on the models of different v_e, the best solution of v_e (along with its probable error) can be established by combining many lines of different K. This technique turned out successful, and in Paper II it was concluded that Sirius A is an intrinsically slow rotator ($16 \leq v_e \lesssim 30$–40 km s^{-1}).

Motivated by this achievement, the author decided to apply this method to analysing the spectral line profiles of Vega, in order to revisit the task of determining its v_e as done in Paper I, hoping that a result of higher accuracy would be obtained, so that the diversified literature values may be verified. The purpose of this article is to report the outcome of this reinvestigation.

2 OBSERVATIONAL DATA

2.1 Selection of lines and their profiles

Regarding the basic observational material of Vega, the high-dispersion spectra of high signal-to-noise ratio (S/N ~ 2000) and high spectral resolving power ($R \sim 100\,000$) were used as in Paper I, which were obtained at Okayama Astrophysical Observatory by using the HIDES spectrograph attached to the 188 cm reflector and published by Takeda, Kawanomoto & Ohishi (2007).

The selection of lines to be used for the analysis was done by following almost the same procedure as adopted in Paper II (cf. section 2.2 therein), where it was decided to employ only lines of neutral and ionized Fe in order to maintain consistency with Paper II. As a result, a total of 90 lines (49 Fe I and 41 Fe II lines) were eventually sorted out,[1] which are listed in Table 2. The observed profiles of these lines are displayed in Fig. 1, and their

---

[1]Since the selection criterion adopted in this study differs from that of Paper I, the resulting line set is somewhat different. More precisely, out of 60/52 Fe I/Fe II lines analysed in Paper I, 17/16 were discarded, while 6/5 were newly included.

Table 2. Atomic data and observed quantities of adopted spectral lines.

λ (Å)	χ_low (eV)	log *gf* (dex)	W^{obs} (mÅ)	K	q_1^{obs} (km^{-1} s)	q_2^{obs} (km^{-1} s)
(49 Fe I lines)						
3922.911	0.052	− 1.651	25.3	− 14.89	0.02465	0.05085
4014.534	3.573	− 0.200	7.6	− 14.48	0.02425	0.05050
4021.867	2.759	− 0.660	9.4	− 15.21	0.02276	0.05120
4067.978	3.211	− 0.430	7.8	− 14.63	0.02393	0.04988
4175.636	2.845	− 0.670	6.4	− 14.82	0.02540	0.05027
4176.566	3.368	− 0.620	5.2	− 15.59	0.02517	0.04823
4187.038	2.449	− 0.548	15.9	− 14.36	0.02398	0.04980
4195.329	3.332	− 0.412	8.3	− 14.90	0.02538	0.04882
4196.208	3.396	− 0.740	4.2	− 14.73	0.02371	0.04530
4199.095	3.047	+ 0.250	26.5	− 12.26	0.02503	0.05200
4202.028	1.485	− 0.708	33.6	− 12.38	0.02477	0.05236
4210.343	2.482	− 0.870	7.8	− 15.85	0.02426	0.05217
4219.360	3.573	+ 0.120	15.4	− 13.31	0.02362	0.04897
4235.936	2.425	− 0.341	21.6	− 13.69	0.02568	0.05155
4238.021	3.417	− 1.286	2.7	− 15.76	0.02373	0.04730
4238.809	3.396	− 0.280	9.8	− 14.59	0.02490	0.05084
4299.234	2.425	− 0.430	21.1	− 13.56	0.02584	0.05010
4447.718	2.223	− 1.342	5.9	− 16.05	0.02342	0.04301
4466.551	2.832	− 0.590	12.4	− 14.96	0.02520	0.05088
4484.219	3.602	− 0.720	3.4	− 15.35	0.02078	0.04992
4494.563	2.198	− 1.136	7.6	− 16.26	0.02423	0.04895
4528.613	2.176	− 0.822	16.3	− 14.93	0.02450	0.05115
4547.846	3.546	− 0.780	2.0	− 16.44	0.02646	0.05141
4602.940	1.485	− 1.950	2.9	− 17.95	0.02107	0.04621
4611.284	3.654	− 0.670	2.8	− 15.21	0.02335	0.04747
4707.272	3.241	− 1.080	2.7	− 15.76	0.02289	0.05004
4903.308	2.882	− 1.080	3.9	− 15.85	0.02487	0.05074
4918.993	2.865	− 0.370	14.0	− 14.24	0.02469	0.05088
4920.502	2.832	+ 0.060	29.3	− 12.08	0.02636	0.05265
4966.087	3.332	− 0.890	3.7	− 16.69	0.02211	0.05162
5049.819	2.279	− 1.420	4.7	− 17.23	0.02071	0.04464
5133.681	4.178	+ 0.140	10.0	− 13.76	0.02473	0.05017
5162.292	4.178	+ 0.020	8.7	− 14.23	0.02422	0.04991
5281.790	3.038	− 1.020	4.0	− 15.46	0.02387	0.04728
5341.023	1.608	− 2.060	3.5	− 17.63	0.02246	0.06592
5353.373	4.103	− 0.840	1.5	− 15.53	0.02327	0.04369
5364.858	4.446	+ 0.220	7.5	− 13.94	0.02370	0.05068
5367.479	4.415	+ 0.350	9.3	− 13.76	0.02557	0.05168
5371.489	0.958	− 1.645	12.3	− 16.95	0.02419	0.04971
5389.479	4.415	− 0.410	1.9	− 15.21	0.02572	0.04028
5569.618	3.417	− 0.540	4.5	− 15.87	0.02460	0.05192
5572.841	3.396	− 0.310	7.6	− 15.01	0.02508	0.05084
5576.090	3.430	− 1.000	2.2	− 14.98	0.02342	0.04979
5615.644	3.332	− 0.140	14.3	− 14.33	0.02563	0.05133
5633.975	4.991	− 0.270	1.6	− 14.59	0.02282	0.04763
6136.615	2.453	− 1.400	3.8	− 17.28	0.02402	0.04708
6137.694	2.588	− 1.403	2.8	− 18.58	0.02271	0.04905
6191.558	2.433	− 1.600	2.8	− 18.58	0.02341	0.04736
6230.726	2.559	− 1.281	4.0	− 16.44	0.02328	0.05124
(41 Fe II lines)						
4273.326	2.704	− 3.258	17.2	− 5.30	0.02662	0.05143
4278.159	2.692	− 3.816	7.2	− 5.98	0.02611	0.05284
4296.572	2.704	− 3.010	32.6	− 4.28	0.02764	0.05285
4413.601	2.676	− 3.870	4.2	− 5.66	0.02780	0.04958
4451.551	6.138	− 1.844	8.1	− 1.19	0.03020	0.05623
4472.929	2.844	− 3.430	13.2	− 5.45	0.02412	0.05491
4489.183	2.828	− 2.970	31.7	− 4.54	0.02730	0.05278
4491.405	2.855	− 2.700	38.5	− 4.12	0.02813	0.05322
4541.524	2.855	− 3.050	27.7	− 4.68	0.02737	0.05199
4576.340	2.844	− 3.040	27.6	− 4.70	0.02744	0.05185
4582.835	2.844	− 3.100	19.4	− 5.20	0.02645	0.05223

Table 2 *– continued*

λ (Å)	χ_low (eV)	log *gf* (dex)	W^{obs} (mÅ)	K	q_1^{obs} (km^{-1} s)	q_2^{obs} (km^{-1} s)
4620.521	2.828	− 3.280	15.8	− 5.16	0.02702	0.05118
4635.316	5.956	− 1.650	15.6	− 1.54	0.03032	0.05428
4666.758	2.828	− 3.330	16.4	− 5.56	0.02623	0.05034
4713.193	2.778	− 4.932	5.9	− 6.53	0.03818	0.06809
4731.453	2.891	− 3.360	20.9	− 5.29	0.02692	0.05184
4913.292	10.288	+ 0.012	2.0	+ 4.82	0.03830	0.08123
4948.793	10.347	− 0.008	1.9	+ 5.07	0.03419	0.06236
4951.584	10.307	+ 0.175	3.3	+ 2.92	0.03701	0.05541
4977.035	10.360	+ 0.041	2.1	+ 4.59	0.03409	0.05122
4993.358	2.807	− 3.650	8.4	− 6.27	0.02610	0.05199
5089.214	10.329	− 0.035	2.5	+ 3.85	0.02708	0.04168
5106.109	10.329	− 0.276	1.1	0.00	0.04118	0.08262
5127.866	5.570	− 2.535	3.7	− 2.60	0.02657	0.07004
5132.669	2.807	− 4.180	3.1	− 6.21	0.02566	0.05284
5149.465	10.447	+ 0.396	5.3	+ 3.63	0.02978	0.04636
5203.638	10.391	− 0.046	1.9	+ 5.07	0.02968	0.05292
5219.926	10.522	− 0.366	1.2	+ 3.85	0.02856	0.04502
5272.397	5.956	− 2.030	7.0	− 2.05	0.02980	0.04995
5291.666	10.480	+ 0.575	5.1	+ 2.80	0.03584	0.07705
5387.063	10.521	+ 0.518	4.4	+ 3.25	0.03395	0.05187
5529.932	6.729	− 1.875	3.5	− 1.36	0.02854	0.05276
5567.842	6.730	− 1.887	2.1	0.00	0.03195	0.05079
5645.392	10.561	+ 0.085	1.9	+ 5.07	0.03955	0.05893
5835.492	5.911	− 2.372	1.4	0.00	0.02289	0.04158
6084.111	3.199	− 3.808	4.0	− 7.22	0.02622	0.05076
6147.741	3.889	− 2.721	14.4	− 5.00	0.02691	0.05213
6149.258	3.889	− 2.724	14.0	− 5.14	0.02678	0.05177
6175.146	6.222	− 1.983	4.0	− 2.41	0.02596	0.04678
6248.898	5.511	− 2.696	3.2	− 3.01	0.02396	0.04336

Note. In columns 1–7 are given the line wavelength, lower excitation potential, logarithm of oscillator strength times lower level's statistical weight, observed equivalent width, *T*-sensitivity parameter, observed first zero frequency, and observed second zero frequency, respectively. The atomic data are taken from the compilation of Kurucz & Bell (1995).

original data are available in 'obsprofs.dat' of the supplementary material.

The equivalent widths (W^{obs}) of these 90 lines were measured by the Gaussian fitting method, which are in the range of 1 mÅ $\lesssim W^{obs} \lesssim$ 40 mÅ. As the 'standard' plane-parallel model atmosphere for Vega, Kurucz's (1993) ATLAS9 model with T_{eff} = 9630 K, log g = 3.94, v_t = 2 km s^{-1} (microturbulence), and [X/H] = −0.5 (metallicity) was adopted in this study as in Paper I, which well reproduces the spectral energy distribution. By using this model along with the atomic data taken from Kurucz & Bell (1995)'s compilation, the abundance (A^{std}; called as 'standard abundance') was derived from W^{obs} for each line.

In the same manner as in Paper II (cf. section 4.1 therein), the *T*-sensitivity parameter K ($\equiv$ dlog *W*/dlog *T*) was then evaluated as

$$K \equiv \frac{(W^{+100} - W^{-100})/W^{obs}}{(+100 - (-100))/9630}, \qquad (1)$$

where W^{+100} and W^{-100} are the equivalent widths computed from A^{std} by two model atmospheres with only T_{eff} being perturbed by +100 K (T_{eff} = 9730 K) and −100 K (T_{eff} = 9530 K), respectively (while other parameters are kept the same as the standard values). The ranges of the resulting K values are (roughly) $-20 \lesssim K \lesssim -10$ and $-5 \lesssim K \lesssim +5$ for Fe I and Fe II lines, respectively.
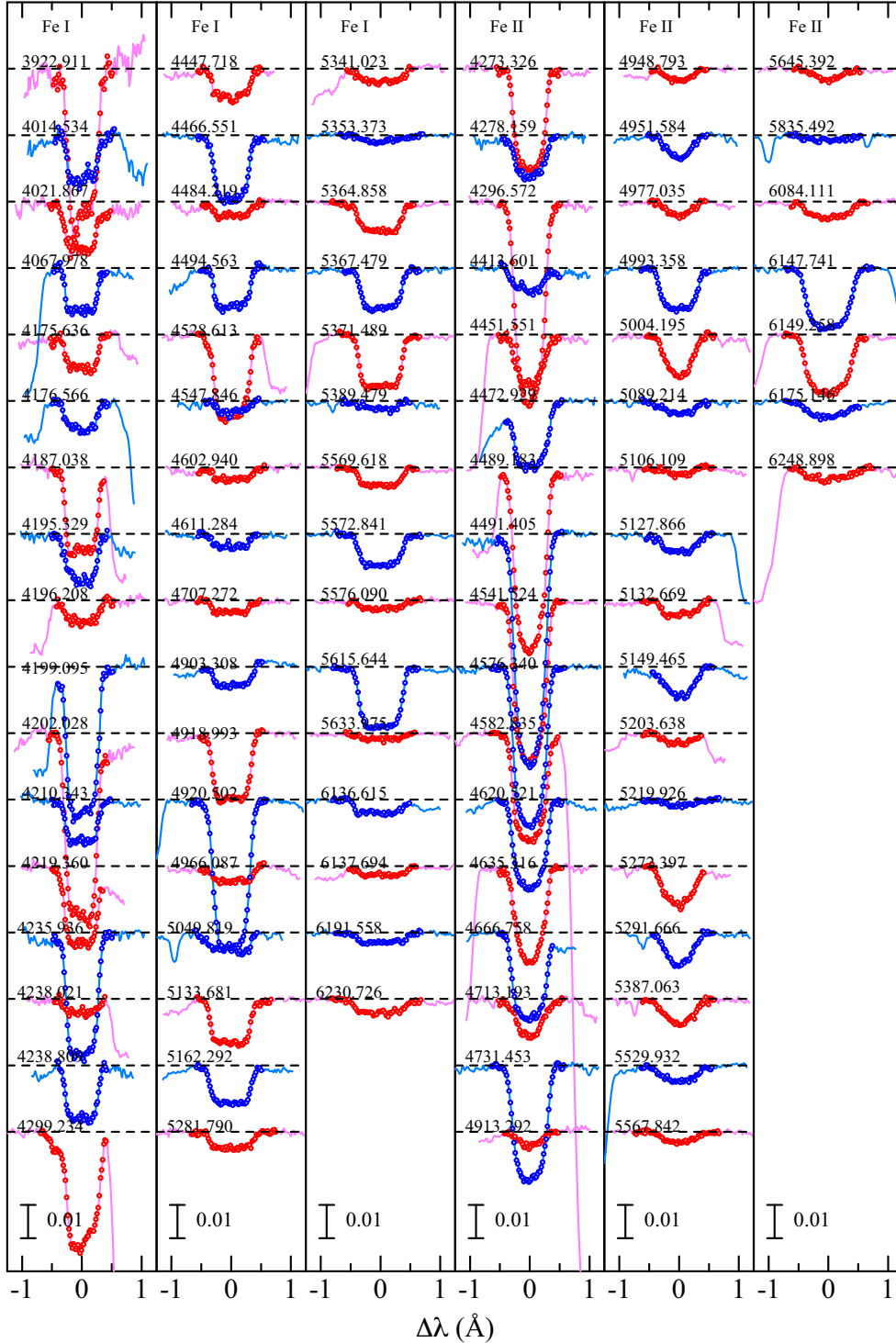
Figure 1. Observed spectra of finally selected 49 Fe I lines (first through third panels) and 41 Fe II lines (fourth through sixth panels), which are arranged in the increasing order of wavelength within each group of species as in Table 2. The actual spectral data (normalised flux plotted against the wavelength displacement relative to the line centre) are shown by lines, while the selected wavelength portions [λ_1, λ_2] used for calculating the Fourier transforms are depicted by symbols. Each spectrum (its continuum level is indicated by the horizontal dashed line) is shifted by 0.02 (2 per cent of the continuum level) relative to the adjacent one.

2.2 Zero frequencies of Fourier transforms

Then, the Fourier transform $d(\sigma)$ of the line depth profile D_λ ($\equiv 1 - F_\lambda/F_{cont}$) was calculated for each line as done in Paper II (cf. section 2.3 therein), and the first and second zero frequencies (σ_1 and σ_2, in unit of wavelength^{-1}) were measured from the cuspy features

of $|d(\sigma)|$, which were further converted to wavelength-independent quantities (q_1 and q_2, in unit of velocity^{-1}) for convenience by the relation $q \equiv \sigma(\lambda/c)$ (c: velocity of light). The resulting q_1 and q_2 are plotted against the line parameters in Fig. 2, from which the following arguments can be made:
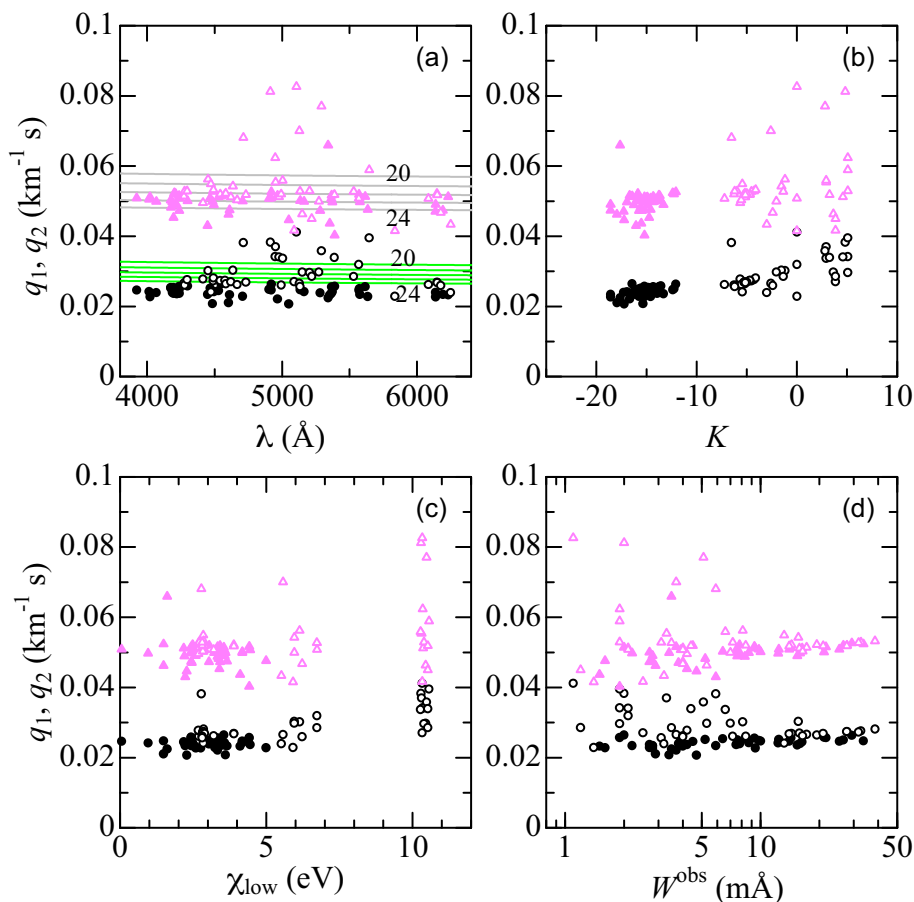
Figure 2. The first zero frequencies (q_1: circles) and second zero frequencies (q_2: triangles) of Fourier transforms, which were calculated from the observed profiles of 90 Fe lines, are plotted against (a) λ (wavelength), (b) K (*T*-sensitivity parameter), (c) χ_{low} (lower excitation potential), and W^{obs} (observed equivalent width). The filled and open symbols correspond to Fe I and Fe II lines, respectively. In panel (a), the classical $q_1(\lambda)$ and $q_2(\lambda)$ values derived from the conventional rotational broadening function corresponding to $v_e \sin i = 20, 21, 22, 23,$ and 24 km s^{-1} (which were derived from equations 3, 4, and 6 in Paper II) are depicted by solid lines.

(i) These zero frequencies show an appreciable line-dependent scatter; especially, those of a fraction of Fe II lines are remarkably higher in comparison with the theoretical values expected from the classical rotational broadening function (cf. Fig. 2a)

(ii) This implies that the conventional Fourier analysis of spectral line profiles, which assumes that the observed profile is expressed by a convolution of the rotational broadening function and thus the zero frequency of the rotational broadening function (dependent on $v_e \sin i$) should be simply inherited in the observed transform equally for any line, is no more applicable for precise $v_e \sin i$ determination in this case.

(iii) The cause for this scatter in q_1 as well as q_2 is that they tend to systematically increase with K as shown in Fig. 2(b). This is because the line profile characteristics are determined by this *T*-sensitivity parameter; that is, a line of small/negative K (e.g. weak Fe I line of low excitation) shows a boxy **U**-shape, while that of large/positive K (e.g. weak Fe II line of high excitation) has a sharp **V**-shape. Such a difference in the line profile (even if very subtle) is reflected by the position of zero frequency, which is actually verified by theoretical calculations based on the gravity-darkened rotating star model (cf. Section 3.3).

(iv) These q_1 and q_2 also show some systematic trends with respect to χ_{low} (Fig. 2c) and W^{obs} (Fig. 2d); however, they can be reasonably explained by the dependence of K on χ_{low} and W^{obs}, as discussed in

appendix A2 of Paper II. Accordingly, it is the difference in K that causes the line-by-line different characteristics in the profile (and the zero positions).

The atomic line data and the values of W^{obs}, K, q_1, and q_2 for 90 lines are presented in Table 2. Besides, more complete data (including A^{std} and the main lobe height as well as the first sidelobe height) are summarised in 'obsparms.dat' of the supplementary material.

3 MODELLING OF LINE PROFILES

3.1 Adopted model parameters

Regarding the simulation of theoretical line profiles of a gravity-darkened rotating star, this study follows the same assumptions and procedures (including the adopted set of parameters for Vega) as described in Paper I, where the stellar mass (M), rotational velocity at the equator (v_e), inclination angle of rotation axis (i), polar radius (R_p), and polar effective temperature ($T_{eff,p}$) are the fundamental parameters to be specified.

The mass was fixed at $M = 2.3$ M$_\odot$. 10 v_e values were chosen as 22, 100, 125, 150, $\cdots$ 275, and 300 km s^{-1} (numbered as models 0, 1, 2, 3, $\cdots$, 8, and 9), and the corresponding i values were derived from the assumption of $v_e \sin i = 22$ km s^{-1} (which is a reasonable value

Table 3. Parameters of adopted models for rotating Vega.

Model number	v_e (km s^{-1})	i (deg)	R_p (R$_\odot$)	R_e (R$_\odot$)	$T_{\rm eff,p}$ (K)	$T_{\rm eff,e}$ (K)	$\log g_p$ (cm s^{-2})	$\log g_e$ (cm s^{-2})	Remark
0	22	90.0	2.700	2.700	9630	9630	3.937	3.937	Gravity effect suppressed.
1	100	12.7	2.640	2.722	9698	9399	3.956	3.956	–
2	125	10.1	2.600	2.726	9750	9281	3.969	3.884	–
3	150	8.4	2.560	2.740	9806	9126	3.983	3.858	–
4	175	7.2	2.520	2.763	9867	8931	3.997	3.823	Nominated model in Paper I.
5	200	6.3	2.470	2.784	9932	8695	4.014	3.783	Best model concluded in this study.
6	225	5.6	2.410	2.799	10000	8416	4.035	3.736	–
7	250	5.0	2.360	2.837	10074	8072	4.054	3.669	–
8	275	4.6	2.300	2.869	10151	7787	4.076	3.587	–
9	300	4.2	2.240	2.908	10233	7546	4.099	3.477	–

Note. Given are the model number, equatorial rotation velocity, inclination angle, radius, effective temperature, and logarithmic surface gravity at the pole as well as the equator. These models are the same as adopted in Paper I (cf. table 1 therein). Note that $v_e \sin i$ is assumed to be 22 km s^{-1} in all these models.

for Vega). Based on the requirement of spectral energy distribution, R_p and $T_{\rm eff,p}$ can be expressed as second-order polynomials in terms of v_e (cf. equations 1 and 2 in Paper I). The model parameters for each of the 10 models are summarised in Table 3, which is the same as table 1 in Paper I. Note that model 0 ($v_e = 22$ km s^{-1} and $i = 90°$) is a special model different from others, in the sense that it is a spherically symmetric rigid model where the gravity effect (darkening and distortion) is intentionally suppressed. This model 0 is almost equivalent to the 'standard model' mentioned in Section 2.1.

3.2 Simulation of line profiles

The emergent line flux profile was simulated with the program CALSPEC (cf. section 4.1 in Paper I) by integrating the intensity profile at each point on the visible disc, which was generated by using the local model atmosphere corresponding to $T_{\rm eff}(\Theta)$, $g(\Theta)$, $v_t = 2$ km s^{-1}, and [X/H] $= -0.5$ (where Θ is the co-latitude).

Here, a point to notice is how to assign the elemental abundance (A). If $A^{\rm std}$ (standard abundance derived from the classical plane-parallel model) is simply used, the equivalent width of the calculated line profile ($W^{\rm cal}$) turns out generally stronger than $W^{\rm obs}$ because of the gravity darkening effect,[2] and this discrepancy progressively increases towards higher v_e (as can be recognized in figs 4 and 5 in Paper I). In Paper I, this problem was circumvented by renormalising the calculated profile (cf. equation 7 therein) so as to force $W^{\rm cal} = W^{\rm obs}$, although its validity was not necessarily clear.

Fortunately, this equality does not have to be strictly realised in the present case of Fourier analysis, because it is the 'characteristics' of the line shape that are essential. Accordingly, the following procedure was adopted in this study:

(i) First, the provisional equivalent width W_*^j ($j = 0, 1, 2, \cdots, 9$) was calculated with CALSPEC for each model by using $A^{\rm std}$.

(ii) Then, the corresponding abundance A_*^j was derived from W_*^j with the help of Kurucz (1993)'s WIDTH9 program by using the standard plane-parallel model (cf. Section 2.1).

(iii) The abundance difference defined as $\Delta A^j \equiv A^{\rm std} - A_*^j$ (which is mostly negative) is used as abundance correction to be

applied to $A^{\rm std}$; that is, the abundance actually adopted in CALSPEC for calculating the profile corresponding to model j is $A^{\rm std} + \Delta A^j$.

It should be remarked that this procedure is based on two assumptions that (i) the classical curve of growth ($\log W$ versus A relation) for the plane-parallel model is applicable even for the gravity-darkened case, and (ii) the absolute change of $\log W$ in response to perturbation by $\pm \Delta A$ around $A^{\rm std}$ in this curve of growth is almost the same (i.e. locally linear). Despite these rough approximations, the discrepancy between $W^{\rm cal}$ and $W^{\rm obs}$ seen for the case of simply using $A^{\rm std}$ is considerably reduced by application of this correction (ΔA), as shown in Fig. 3.

### 3.3 Fourier transform and the trend of first zero

By using such corrected abundances, the theoretical line profiles were simulated for each of the 10 models and their Fourier transforms were computed, from which q_1^j and q_2^j ($j = 0, 1, 2, \cdots, 9$) were measured. These q_1^j and q_2^j values along with the adopted abundance corrections (ΔA^j) for all 90 lines are given in 'calparms.dat' of the supplementary material.

As demonstrative examples, the simulated profiles of Fe I 5133.681 ($K = -13.76$) and Fe II 4951.584 ($K = +2.92$) lines and their Fourier transform amplitudes, which were calculated for models 0, 1, 3, 5, 7, and 9, are illustrated in Fig. 4, where the observed data are also overplotted for comparison. It can be seen from Fig. 4 that the behaviours of zero frequency for these two lines of different K are just the opposite in the sense that q_1 of Fe I 5133.681/Fe II 4951.584 moves towards lower/higher direction as the gravity darkening effect is enhanced with an increase in v_e.

From now on, our discussion focuses only on the first zero frequency (q_1), which is less affected by measurement errors or noises in comparison to q_2. In order to elucidate the trend of q_1 as a function of K and v_e, the q_1 values are plotted against K in Figs 5(a)–(f) (each corresponding to models 0, 1, 3, 5, 7, and 9, respectively). Besides, the linear regression lines (determined from the q_1 versus K plots for Fe I and Fe II lines separately) are also shown in each panel, and these regression lines for all models are depicted together in Fig. 5(g). An inspection of Fig. 5 reveals the following characteristics:

(i) q_1 generally increases with an increase in K, which was already mentioned in Section 2.2 in reference to Fig. 2(b). The q_1 values for Fe I lines are generally smaller than those of Fe II lines because of the difference in K.

---

[2]Although $A^{\rm std}$ was simply used in Paper II for all models irrespective of v_e, it did not cause any serious problem because v_e-dependent gravity darkening effect was not so large as to cause a significant $W^{\rm cal}$ versus $W^{\rm obs}$ discrepancy in the v_e range (≤ 150 km s^{-1}) inspected therein.
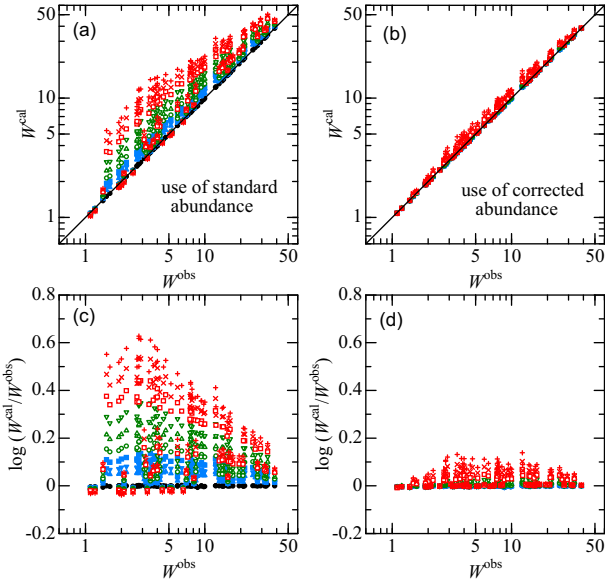
Figure 3. Graphical illustration describing how the abundance correction applied to the standard abundance (cf. Section 3.2) improves the discrepancy between the observed (W^{obs}) and calculated (W^{cal}) equivalent widths for each line, where W^{cal} (upper panels) and $\log(W^{cal}/W^{obs})$ (lower panels) are plotted against W^{obs}. The left-hand panels (a, c) correspond to the case of using the standard (uncorrected) abundances, while the right-hand panels (b, d) correspond to the case of using the corrected abundances. The results for models 0, 1, 2, 3, 4, 5, 6, 7, 8, and 9 are denoted by filled circles, filled triangles, filled inverse triangles, filled squares, open circles, open triangles, open inverse triangles, open squares, St. Andrew's crosses ($\times$), and Greek crosses ($+$), respectively. (The symbols for model 0, models 1–3, models 4–6, and models 7–9 are coloured in black, blue, green, and red, respectively.)

(ii) The slope of the q_1 versus K plots is a systematic function of v_e; i.e. it becomes progressively steeper with an increase in v_e (Fig. 5g). This is a useful property for estimating v_e from the observed q_1–K relation.

(iii) The sensitivity of q_1 to a change in v_e also depends on K (cf. Fig. 5h). While $\langle dq_1/dv_e \rangle \lesssim 0$ holds for most lines of $K \lesssim 0$ (all Fe I lines and many Fe II lines), a group of high-excitation Fe II lines ($\chi_{low} \sim 10$ eV; such as Fe II 4951.584 in Fig. 4) with positive K indicates $\langle dq_1/dv_e \rangle > 0$.

4 RESULT AND DISCUSSION

4.1 Rotational velocity of Vega

Now that the observational data of zero frequencies (q_1^{obs}) as well as the corresponding theoretically calculated values ($q_1^{cal,j}$ for $j = 0, 1, \cdots, 9$) to be compared are all set for 90 lines, we can address the main task of investigating Vega's rotational velocity, while following the same procedure as adopted in Paper II (cf. section 4.3 therein).

The observed q_1^{obs} values are plotted against K in Fig. 6. As seen from this figure, these q_1^{obs} data show an increasing tendency with K and those for Fe I and Fe II lines are distributed in separate two groups, which is quite similar to the theoretical predictions mentioned in Section 3.3 (cf. Figs 5a–f). Therefore, there is a good hope of successfully establishing v_e by comparing q_1^{obs} and q_1^{cal} for many lines altogether.

Since the actual value of $v_e\sin i$ (hereinafter denoted as x for simplicity) is likely to be slightly different from 22 km s^{-1} assumed

for calculating the modelled profiles, $q_1^{th,j}$ should be multiplied by a scaling factor ($22/x$) to allow for this possible difference. The standard deviation defined as

$$\sigma\left(x^i, v_e^j\right) \equiv \sqrt{\frac{\sum_{n=1}^{N}\left[q_1^{obs}(n) - q_1^{cal,j}(n)(22/x^i)\right]^2}{N}} \quad (2)$$

was computed for each combination of (x^i, v_e^j), where $x^i = 15.0 + 0.2i$ ($i = 0, 1, \cdots, 75$) and $v_e^j = 100 + 25(j-1)$ ($j = 1, 2, \cdots, 9$). Here, n is the index of each line and N is the total number of the lines used. As in Paper II, Fe I lines ($N = 49$) and Fe II lines ($N = 41$) are treated separately. The best (x, v_e) solution may be found by searching for the location of σ minimum.

The behaviours of the resulting σ (3D surface and contour plots) are displayed in Fig. 7 (left- and right-hand panels are for Fe I and Fe II, respectively). The trace line connecting (x^*, v_e) is also overplotted by the dashed line, where x^* corresponds to the minimum of σ trough for each v_e (in Table 4 are given the actual data of x^* and the corresponding σ^*). Besides, the run of σ with v_e across the tracing is depicted in Fig. 8(a), and the tracings for both species are drawn together in Fig. 8(b).

An inspection of Fig. 8 yielded satisfactory results, because three kinds of (x, v_e) solutions turned out consistent with each other: (191, 21.8) from the minimum of σ_I (Fig. 8a), (194, 21.5) from the minimum of σ_{II} (Fig. 8a), and (201, 21.5) from the intersection of two trace lines (Fig. 8b).

The uncertainties involved in x^* were estimated as ~ 0.14 km s^{-1} (Fe I) and ~ 0.36 km s^{-1} (Fe II),[3] which are indicated by dashed lines in Fig. 8(b). From this figure, errors in v_e and x were roughly evaluated (from the size of the parallelogram area embraced by four dashed lines around the intersection) as $\sim \pm 15$ km s^{-1} and $\sim \pm 0.3$ km s^{-1}, respectively.

Consequently, by averaging these three solutions, Vega's equatorial and projected rotational velocities were concluded as $v_e = 195(\pm 15)$ km s^{-1} and $v_e\sin i = 21.6(\pm 0.3)$ km s^{-1}, which further result in $i = 6.4°(\pm 0.5°)$. Among the 10 models adopted in this study (cf. Table 3), model 5 ($v_e = 200$ km s^{-1}) is the most preferable model; this can be actually confirmed in Fig. 6, where the linear-regression lines defined in Fig. 5(b)–(f) are overplotted (after the v_e-dependent difference between x^* and 22 has been corrected).

4.2 Comparison with previous results

As mentioned in Section 1, although the considerably large differences of Vega's v_e amounting to $\gtrsim 100$ km s^{-1} seen in the literature of early time were reduced in the more recent results (most of them were published within several years around 2010), they are still diversified ranging from ~ 170 to ~ 230 km s^{-1}. Interestingly, the v_e value (~ 200 km s^{-1}) derived in this study is almost in-between this dispersion. It may be worth briefly reviewing these literature v_e values (published since Paper I; cf. Table 1) in comparison with the consequence of this investigation.

(i) Line profile method:
Paper I's result (175 km s^{-1}) based on the conventional profile fitting has been revised upwards by $\sim +20$ km s^{-1} in this reinvestigation by applying the Fourier transform method to line profiles. While Yoon et al. (2010)'s 236 km s^{-1} is somewhat too large, Hill, Gulliver &

---

[3]This estimation is based on the relation $\delta x/x \sim \delta q_1/q_1$, where $\delta q_1 \sim \sigma/\sqrt{N}$. See section 4.3 in Paper II for more details.
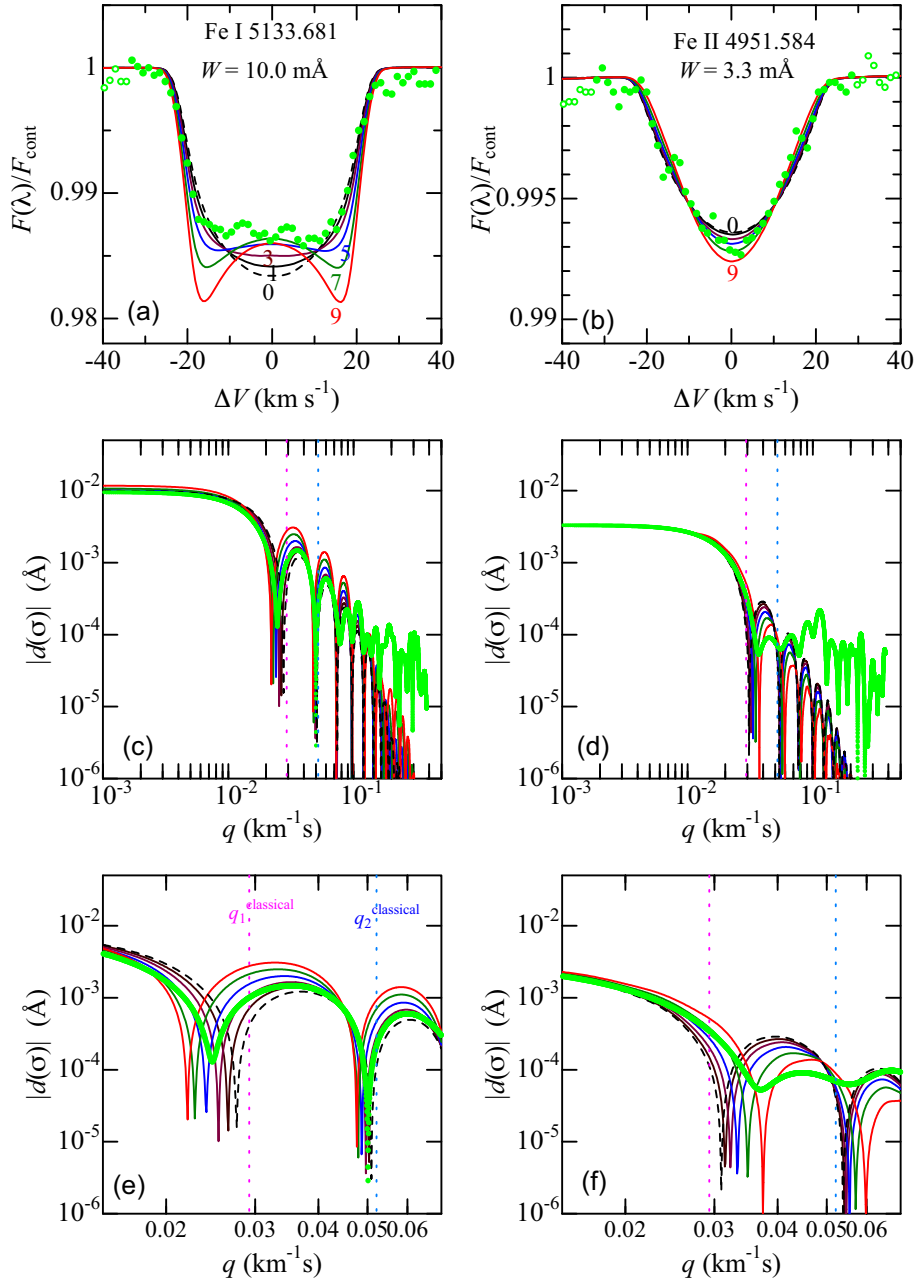
Figure 4. Theoretical line profiles (top panels) and their Fourier transform amplitudes (middle/bottom panels for wide/zoomed view) of Fe I 5133.681 (left-hand side) and Fe II 4951.584 (right-hand side) calculated for models 0 (black dashed line), 1 (black solid line), 3 (purple solid line), 5 (blue solid line), 7 (green solid line), and 9 (red solid line); the observed data are also overplotted by light green symbols. In the middle/bottom panels, the positions of $q_1^{\text{classical}}$ and $q_2^{\text{classical}}$ corresponding to the classical rotational broadening function (cf. equations 3, 4, and 6 in Paper II) are indicated by vertical dotted lines for comparison.

Adelman ([2010](#))'s 211 km s^{-1} is in tolerable agreement as compared with the present result.

(ii) Interferometry method:
Monnier et al. ([2012](#))'s conclusion of $v_e = 197$ km $^{-1}$ (derived from $v_e \sin i$ and i given in their table 2 as Model 3) based on optical interferometry is in good agreement with this study. Actually, fig. 2 of Monnier et al. ([2012](#)) shows that their Model 3 matches well with model 5 ($v_e = 200$ km s^{-1}) of Paper I.

(iii) Magnetic modulation method:
Vega's rotational period (P) was directly determined by way of detecting the magnetic modulation based on time-sequence data of spectropolarimetric observations: 0.732 d (Petit et al. [2010](#)), 0.678 d

(Alina et al. [2012](#)), 0.623 d (Butkovskaya [2014](#)), and 0.678 d (Böhm et al. [2015](#)). Among these four, it is the P-value of 0.678 d derived by both Alina et al. and Böhm et al. that is most consistent with the v_e result (195 km s^{-1}) of this investigation, which corresponds to $P = 2\pi R_e/v_e = 0.685$ d (where $R_e = 2.784$ R$_\odot$ for model 5 is adopted).

4.3 Advantage of Fourier analysis

Finally, some comments may be in order regarding the superiority of exploiting the zero frequency (q_1) measured from the Fourier transform of line profiles in comparison with the ordinary profile fitting approach in the wavelength domain.
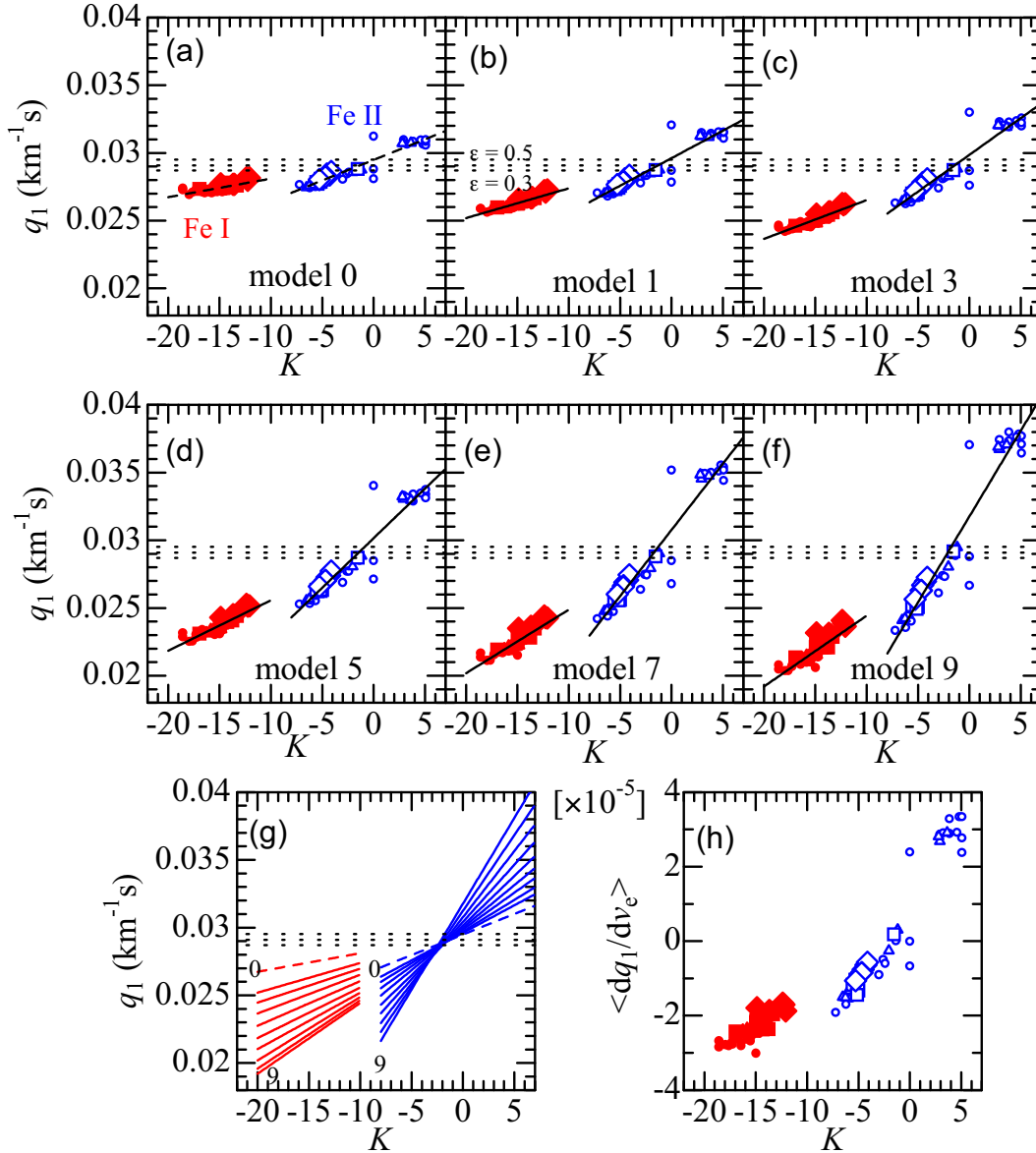
Figure 5. Panels (a)–(f) show the simulated relationships between q_1 (first zero frequency) and K (T-sensitivity parameter) for the 49 Fe I (red filled symbols) and 41 Fe II lines (blue open symbols) calculated for models 0, 1, 3, 5, 7, and 9, respectively. The size and shape of the symbols denote the difference in line strengths: circles ⋯ $W^{obs} < 5$ mÅ, triangles ⋯ 5 mÅ $\leq W^{obs} < 10$ mÅ, squares ⋯ 10 mÅ $\leq W^{obs} < 20$ mÅ, and diamonds ⋯ 20 mÅ $\leq W^{obs} < 40$ mÅ. The linear regression lines derived from these q_1 versus K plots (separately for Fe I and Fe II) are also overplotted by solid lines in each of the panels (a)–(f), and those for all 10 models are put together in panel (g). The three horizontal dotted lines represent the classical q_1 values (corresponding to $v_e \sin i = 22$ km s^{-1}) for the limb-darkening coefficient (ϵ) of 0.3, 0.4, and 0.5 (cf. equation 3 in Paper II). In panel (h) are plotted the mean gradients $\langle dq_1/dv_e \rangle$ (in unit of km^{-2} s^2; averaged over v_e between 100 and 300 km s^{-1}) against K, which were computed from the coefficients of quadrature fit ($q_1 = A + Bv_e + Cv_e^2$) as $B + 2C \times (100 + 300)/2$ (i.e. dq_1/dv_e at the mid-v_e).

The distinct merit of using q_1 is that it can discern very subtle differences in the profile shape. Fig. 4 provides a good demonstrative example. While the profile of Fe I 5133.681 undergoes a comparatively easy-to-detect change with an increase in v_e (Fig. 4a), that of Fe II 4951.584 is apparently inert (Fig. 4b), which means that getting information on v_e from the profile of the latter is more difficult (this is the reason why Fe II lines could not be used for determining v_e in Paper I). However, the situation is different in the Fourier space, where the shift of q_1 (reflecting the change of line profile) is sufficiently detectable with almost the same order of magnitude for

both cases (cf. Figs 4e and f). Accordingly, Fe I as well as Fe II lines are equally usable for v_e determination if q_1 is invoked, as done in this study.

Besides, q_1 is precisely measurable and easy to handle as a single parameter, which is a definite advantage from a practical point of view. Actually, q_1 data of many lines can be so combined as to improve the precision of v_e (while statistically estimating its error) as done in this paper. Such a treatment would be difficult in the conventional approach of fitting the observed and theoretical profiles.
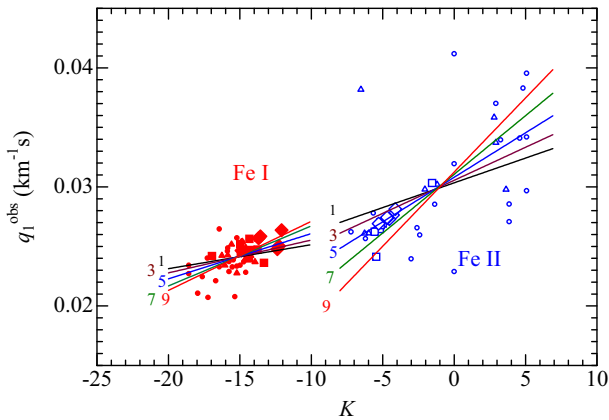
Figure 6. Observed q_1 values of Fe I and Fe II lines plotted against K, where the meanings of the symbols are the same as in Fig. 5. The averaged trends (gradients) of theoretical q_1 versus K relations calculated for models 1, 3, 5, 7, and 9 (determined by linear-regression analysis; cf. Fig. 5) are also depicted by solid lines, which were multiplied by a scaling factor of $22/x^*$ in order to adjust the difference between the actual $v_e \sin i$ ($\equiv x$) and the assumed value (22 km s^{-1}) in the profile calculation (see Table 4 for the v_e-dependent values of x^*).

4.4 Line profile classification using q_1 and K

Another distinct merit of q_1 is that it provides us with a prospect for quantitative classification of spectral line shapes founded on a physically clear basis. Since the discovery around ∼1990 that a number of spectral lines in Vega (e.g. weak lines of neutral species) show unusual profiles of square form, there has been a tendency to pay attention to this specific line group (e.g. compilation of flat-bottomed lines in Vega by Monier et al. 2017). However, the actual

Table 4. Behaviours of σ trough for Fe I and Fe II lines.

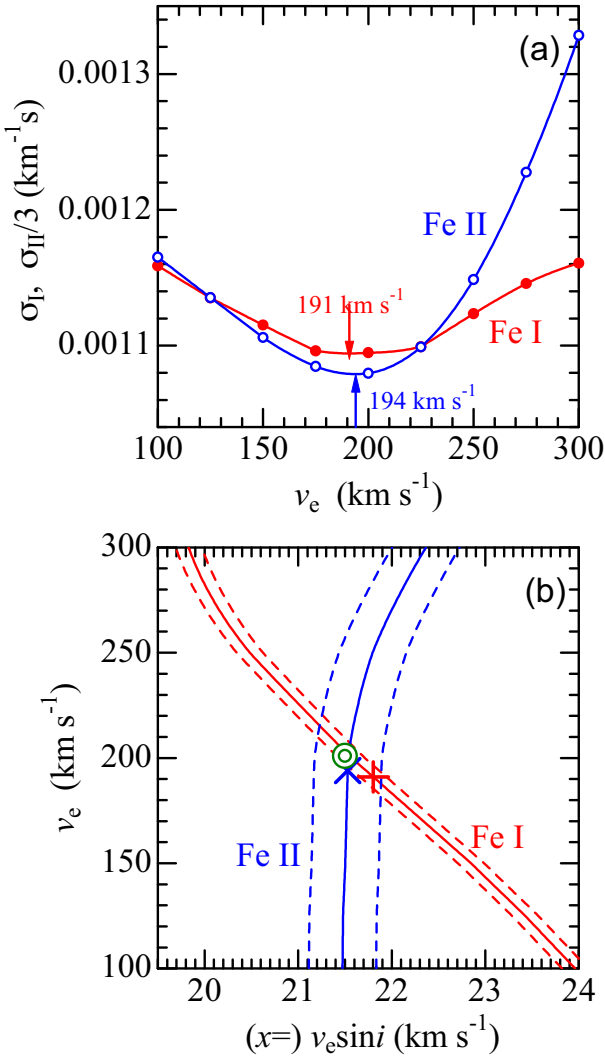| Model number	v_e (km s^{-1})	x_I^* (km s^{-1})	x_{II}^* (km s^{-1})	σ_I^* (km^{-1} s)	σ_{II}^* (km^{-1} s)
1	100	23.9601	21.4741	0.0011587	0.0034953
2	125	23.4263	21.4789	0.0011351	0.0034061
3	150	22.8475	21.5036	0.0011152	0.0033180
4	175	22.2098	21.5175	0.0010961	0.0032541
5	200	21.5720	21.5339	0.0010948	0.0032388
6	225	21.0187	21.6385	0.0010991	0.0032970
7	250	20.4830	21.7954	0.0011235	0.0034459
8	275	20.0921	22.0538	0.0011457	0.0036829
9	300	19.8300	22.3655	0.0011607	0.0039852

Note. These data show the characteristics of the trough in the $\sigma(x, v_e)$ surface ($x \equiv v_e \sin i$) defined by equation (2) for each group of Fe I and Fe II lines. x^* is the x value at the minimum $\sigma(x, v_e)$ for each given v_e, and σ^* is the corresponding $\sigma(x^*, v_e)$. The trace of x^* as a function of v_e is shown by the dashed line in the contour plot of Fig. 7.

situation of Vega's spectral lines in general is not so simple as to be dichotomized into two categories of normal and peculiar profiles; as a matter of fact, the individual profiles of most lines should more or less have anomalies of different degree. Unfortunately, the detection of such details has been hardly possible so far, because the judgement of profile peculiarity was done by simple eye inspection due to the lack of effective scheme for describing/measuring the delicate characteristics of line profiles.

The first zero frequency (q_1) is just what is needed in this context, which is not only sensitive to a slight difference of line shape but also easily measurable in the Fourier space. Moreover, thanks to its close relationship with K, the behaviour of q_1 (representing the line shape characteristics) can be reasonably explained in terms of the underlying physical mechanism. We now have a unified
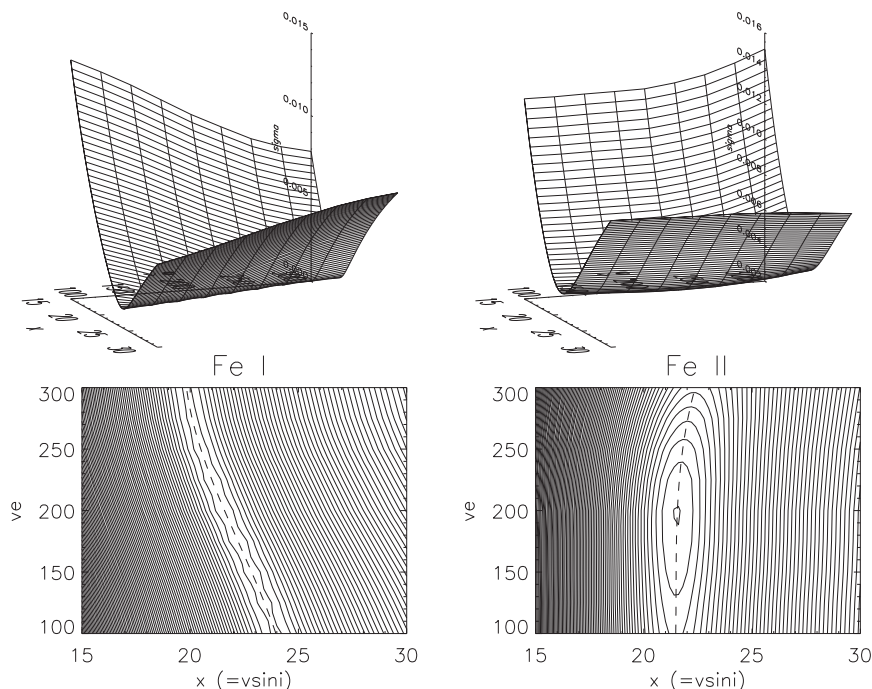
Figure 7. Graphical display of the behaviour of σ, which is the standard deviation between the simulated $q_1^{cal}(x, v_e)$ (where $x \equiv v_e \sin i$) and the observed q_1^{obs} for each of the Fe lines, where the results for Fe I and Fe II lines are separately displayed in the left- and right-hand panels, respectively. Each set consists of the 3D representation of the $\sigma(x, v_e)$ surface (upper panel) and the contours of σ on the x–v_e plane (lower panel). The trace of trough bottom (connection of x^* values at the minimum σ for each given v_e; cf. Table 4) is indicated by the dashed line in the contour plot.

(ii) The peculiarity degree of the line shape (i.e. departure from the classical rotationally broadened profile) is described by K, because $(q_1 - q_1^{classical}) \propto K$ ($q_1^{classical} \simeq 0.03$ km^{-1}s) and the gradient (>0) of this relation progressively increases with v_e, as manifested in Fig. 5. As such, the profile of any line in Vega can be reasonably predicted if K and v_e are specified.

(iii) As explained in appendix A of Paper II, the value of K for each spectral line depends on χ_{low} (lower excitation potential) and W (equivalent width). It is important to note that the line strength affects K in the sense that $|K|$ tends to decrease with an increase in W (i.e. as the line becomes more saturated), which means that chemical abundances are implicitly involved. In the present case of A-type stars, K values for Fe I lines are determined mainly by W, while those for Fe II lines are determined primarily by χ_{low} (cf. fig. A1 in Paper II), which are also indicated from Figs 2(c) and (d).

(iv) These behaviours of K in terms of the line parameters reasonably explain why different spectral lines of Vega reveal various characteristic shapes. For example: (1) Flat-bottom profiles (manifestation of $K < 0$) are seen in Fe I lines but not in Fe II lines, because of the distinct difference in K between these two line groups; i.e. $-20 \lesssim K(\text{Fe I}) \lesssim -10$ and $-5 \lesssim K(\text{Fe II}) \lesssim +5$. (2) The reason why typical flat-bottomed shape is observed mainly in weak Fe I lines (e.g. 4707.272, 4903.308 with W of several mÅ) but not clearly in moderate-strength Fe I lines (e.g. 4202.028, 4920.502 with W of a few tens mÅ) is that the (negative) K values of the former group are generally lower than those of the latter owing to the dependence on W. (3) Regarding Fe II lines, some lines have clearly peaked **V**-shape (e.g. Fe II 5004.195 with $\chi_{low} = 10.272$ eV and $K = +2.92$) while others exhibit rather rounded profile (e.g. Fe II 4993.358 with $\chi_{low} = 2.807$ eV and $K = -6.27$), which is naturally attributed to the apparent distinction of K (the sign is inversed) due to the large difference in χ_{low}.

5 SUMMARY AND CONCLUSION

It is known that the sharp-line star Vega ($v_e \sin i \sim 20$ km s^{-1}) is actually a rapid rotator seen nearly pole-on with low i ($<10°$). However, its intrinsic rotational velocity is still in dispute, for which rather diversified values have been published.

In the previous studies (including Paper I by the author's group), analysis of spectral line profiles has been often invoked for this purpose, which contain information on v_e via the gravity darkening effect, However, it is not necessarily easy to reliably determine v_e by direct comparison of observed and theoretically simulated line profiles. Besides, this approach is not methodologically effective because it lacks the scope for combining many lines in establishing the solution.

Recently, the author applied in Paper II the Fourier analysis to the profiles of many Fe I and Fe II lines of Sirius A and estimated its v_e by making use of the first zero (q_1) of the Fourier transform, which turned out successful. Therefore, the same approach was decided to adopt in this study to revisit the task of establishing v_e of Vega.

As to the observational data, the same high-dispersion spectra of Vega as adopted in Paper I were used. From the Fourier transforms computed from the profiles of selected 49 Fe I and 41 Fe II lines, the corresponding zero frequencies were measured for the analysis. The K values (T-sensitivity parameter) of these Fe lines are in the range of $-20 \lesssim K \lesssim -10$ (Fe I lines) and $-5 \lesssim K \lesssim +5$ (Fe II lines).

Regarding the gravity-darkened models of rotating Vega, the model grid (comprising 10 models) arranged in Paper I was adopted, which cover the v_e range of 100–300 km s^{-1} while assuming $v_e \sin i = 22$ km s^{-1} as fixed. The theoretical profiles of 90 lines were

Figure 8. (a) σ versus v_e relation along the trough bottom for Fe I (filled symbols) and Fe II (open symbols); in each case, the position of minimum σ (evaluated by interpolation) is indicated by an arrow. Note that σ_{II} (σ for Fe II) is reduced by a factor of 1/3 in this figure. (b) The traces of trough bottoms for Fe I and Fe II (dashed lines in the contour panels of Fig. 7) are plotted together in the v_e versus x plane by solid lines (the intersection is shown by the double circle), while the dashed lines indicate the error bars involved in x (± 0.14 km s^{-1} for Fe I and ± 0.36 km s^{-1} for Fe II). The minimum positions of σ_I and σ_{II} are also indicated by Greek cross ($+$) and St. Andrew's cross ($\times$), respectively.

understanding as to why different spectral lines exhibit diversified profiles in Vega, as summarised below.

(i) It is the parameter K (temperature sensitivity) that essentially determines the observed line shape. The contribution to the important shoulder part of the profile away from the line centre ($|\Delta\lambda| \lesssim \lambda v_e \sin i/c$) is mainly made by the light coming from near to the gravity-darkened limb of lowered T. Accordingly, lines of $K < 0$, $K \sim 0$, and $K > 0$ show boxy (**U**-shaped), normally round (like classical rotational broadening), and rather peaked (**V**-shaped) profiles, each of which results in appreciably different q_1 values. For example, in Fig. 4, these three groups correspond to those of lower q_1 (~ 0.025 km^{-1}s), medium q_1 (~ 0.03 km^{-1}s), and higher q_1 (~ 0.035 km^{-1}s), respectively.

simulated for each model, from which Fourier zero frequencies were further evaluated.

An inspection of these q_1^{cal} values for the simulated profiles revealed an increasing tendency with K and the slope of this trend becomes steeper towards larger v_e, which suggests that v_e is determinable by comparing $q_1^{cal}(K, v_e)$ with observed q_1^{obs} for many lines of different K.

It turned out that v_e and $v_e \sin i$ could be separately established by the requirement that the standard deviation of the residual between q_1^{cal} and q_1^{obs} be minimized (while taking into account the difference between the actual $v_e \sin i$ and 22 km s^{-1} assumed in the model profiles), and independent analysis applied to two sets of Fe I and Fe II lines yielded solutions consistent with each other.

The final parameters of Vega's rotation were concluded to be $v_e \sin i$ = 21.6($\pm$0.3) km s^{-1}, v_e = 195($\pm$15) km s^{-1}, and i = 6.4($\pm$0.5)°.

ACKNOWLEDGEMENTS

DATA AVAILABILITY

The data underlying this article are available in the supplementary materials.

REFERENCES

Alina D., Petit P., Lignières F., Wade G. A., Fares R., Aurière M., Böhm T., Carfantan H., 2012, in Hoffman J. L., Bjorkman J., Whitney B., eds, AIP Conf. Proc. Vol. 1429, Stellar Polarimetry: From Birth to Death. Am. Inst. Phys., New York, p. 82

Aufdenberg J. P. et al., 2006, ApJ, 645, 664 (erratum: 651, 617)

Böhm T. et al., 2015, A&A, 577, A64

Butkovskaya V., 2014, in Mathys G., Griffin E., Kochukhov O., Monier R., Wahlgren G., eds, Putting A Stars into Context: Evolution, Environment, and Related Stars. Publ. House 'Pero', Moscow, p. 398

Gulliver A. F., Hill G., Adelman S. J., 1994, ApJ, 429, L81

Hill G., Gulliver A. F., Adelman S. J., 2004, in Zverko J., Žižňovský J., Adelman S. J., Weiss W. W., eds, Proc. IAU Symp. 224, The A-Star Puzzle. Cambridge Univ. Press, Cambridge, p. 35

Hill G., Gulliver A. F., Adelman S. J., 2010, ApJ, 712, 250

Kurucz R. L., 1993, Kurucz CD-ROM, No. 13, ATLAS9 Stellar Atmosphere Program and 2 km/s Grid. Harvard-Smithsonian Center Astrophys., Cambridge, MA

Kurucz R. L., Bell B., 1995, Kurucz CD-ROM, No. 23, Atomic Line List. Harvard-Smithsonian Center Astrophys., Cambridge, MA

Lignières F., Petit P., Böhm T., Aurière M., 2009, A&A, 500, L41

Monier R., Gebran M., Royer F., Kilicoğlu T., 2017, in Reylé C., Di Matteo P., Herpin F., Lagadec E., Lançon A., Meliani Z., Royer F., eds, Proc. Annu. Meeting, SF2A-2017. French Soc. Astron. Astrophys., p.49

Monnier J. D. et al., 2012, ApJ, 761, L3

Peterson D. M. et al., 2006, Nature, 440, 896

Petit P. et al., 2010, A&A, 523, A41

Takeda Y., 2020, MNRAS, 499, 1126 (Paper II)

Takeda Y., Kawanomoto S., Ohishi N., 2007, PASJ, 59, 245

Takeda Y., Kawanomoto S., Ohishi N., 2008a, Contrib. Astron. Obs. Skalnaté Pleso, 38, 157

Takeda Y., Kawanomoto S., Ohishi N., 2008b, ApJ, 678, 446 (Paper I)

Yoon J., Peterson D. M., Kurucz R. L., Zagarello R. J., 2010, ApJ, 708, 71

SUPPORTING INFORMATION

Supplementary data are available at *MNRAS* online.

suppl_data

Please note: Oxford University Press is not responsible for the content or functionality of any supporting materials supplied by the authors. Any queries (other than missing material) should be directed to the corresponding author for the article.

This paper has been typeset from a TEX/LATEX file prepared by the author.